Quantum-limited measurement of magnetic-field gradient with entangled atoms

H. T. Ng
Center for Quantum Information, Institute for Interdisciplinary Information Sciences, Tsinghua University, Beijing 100084, People's Republic of China
(Received 18 January 2013; published 4 April 2013)

We propose a method to detect the amplitude gradient of a microwave field by using a pair of entangled two-component Bose-Einstein condensates. We consider the two spatially separated condensates to be coupled to the two different magnetic fields. The magnetic-field gradient can be determined by measuring the variances of population differences and relative phases between the two-component condensates in two wells. The precision of measurement can reach the Heisenberg limit. We study the effects of one-body and two-body atom losses on the detection. We find that the entangled atoms can outperform the uncorrelated atoms in probing the magnetic fields in the presence of atom losses. The effect of atom-atom interactions is also discussed.

DOI: 10.1103/PhysRevA.87.043602 PACS number(s): 03.75.Gg, 03.75.Dg, 07.55.Ge

I. INTRODUCTION

Probing the magnetic field [1] is important in different areas of science, such as physical science [2], biomedical science [3], etc. Recently, ultracold atoms have been used for detecting magnetic field [4–6] due to long coherence times [7,8] and negligible Doppler broadening. In addition, coherent collisions between atoms lead to nonlinear interactions which can be used to generate quantum entanglement [9]. In fact, entanglement is a useful resource [10] for enhancing the accuracy of precision measurements. The measurements beyond the standard quantum limit have been recently demonstrated [11,12] using entangled atomic Bose-Einstein condensates (BECs).

In this paper, we propose a method to detect the microwave magnetic-field gradient by using two spatially separated condensates of ^{87}Rb atoms, as shown in Fig. 1. Here we consider the two hyperfine spin states of atoms to be coupled to the magnetic fields via their magnetic dipoles [6,13]. Recently, a BEC has been shown to be transported a distance of about 1 mm by using a conveyor belt [14]. Therefore, the two separate condensates can be used for measuring the differences between two magnetic fields at the two different locations. The magnetic-field gradient can be determined by measuring the variances of the population differences and the relative phases between the two-component condensates in the two different wells.

The sensitivity of the detection can be enhanced by using entangled atoms [11,12,15]. Singlet states [16], which are multiparticle entangled states, have been found to be useful for detecting the magnetic-field gradient [17]. The accuracy of measurement can attain the Heisenberg limit [16,17]. In this paper, we discuss how to produce the singlet state of two spatially separated BECs by using entangled tunneling [18] and appropriately applying the relative phase shifts between the atoms. It is necessary to manipulate the tunneling couplings and atom-atom interactions of the condensates in a double well. These have been shown in recent experiments [19–21].

However, the performance of detection can be affected by the atom losses of the condensates [22–24]. In fact, the two-body atom losses [25] are dominant in two-component condensates. We study the effects of one-body and two-body losses on the measurements. We find that the entangled atoms can give better performances than using uncorrelated atoms in detecting the magnetic fields if the loss rates of atoms are much weaker than the coupling strength of the field gradient. Apart from atom losses, the effect of atom-atom interactions on the performance of this detection is also important [26,27]. Here we show that the magnetic-field gradient can be estimated if the nonlinear interactions are sufficiently weak. The accuracy of the detection will be reduced when the strength of nonlinear interactions becomes strong. But this can be minimized by using either Feshbach resonance [11] or a state-dependent trap [12].

II. SYSTEM

We consider two spatially separated BECs of ^{87}Rb atoms, where each atom has two hyperfine levels $|e\rangle = |F = 2, m'_F\rangle$ and $|g\rangle = |F = 1, m_F = -1\rangle$ [6]. Here the magnetic number m'_F of the upper hyperfine level can be $-2, -1$, or 0. This upper state $|e\rangle$ can be carefully chosen for which the polarization of the magnetic field is to be detected [6]. The two BECs are placed above a surface which generates a magnetic-field gradient, as shown in Fig. 1. The two condensates are coupled to the two different magnetic fields via their magnetic dipoles [6,13].

We adopt the two-mode approximation [28] to describe the atoms in deep potential wells. The Hamiltonian H_0 can be written as [18]

$$H_0 = -\frac{\hbar}{2}\left(E_J^e e_L^\dagger e_R + E_J^g g_L^\dagger g_R + \text{H.c.}\right) + \hbar \sum_{\alpha=L,R}\left(U_{ee} n_{e_\alpha}^2 + 2U_{eg} n_{e_\alpha} n_{g_\alpha} + U_{gg} n_{g_\alpha}^2\right), \quad (1)$$

where e_α (g_α) and n_{e_α} (n_{g_α}) are the annihilation and number operators of the atoms in state $|e\rangle$ ($|g\rangle$) in the left and right potential wells, respectively. The parameters E_J^e (E_J^g) and U_{ee} (U_{gg}) are the tunneling strength between the two wells and the atom-atom interaction strength for state $|e\rangle$ ($|g\rangle$), and U_{eg} is the interaction strength between the atoms in the two different components.

We consider the atoms to be resonantly coupled to the microwave magnetic fields. The transition frequencies of hyperfine states can be tuned by a static magnetic field [6]. Here the other hyperfine transitions can be ignored due to

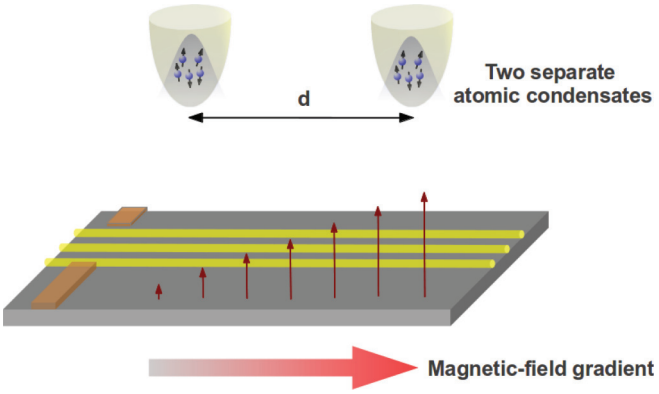

FIG. 1. (Color online) Schematic of two atomic condensates being placed above a surface which produces a magnetic-field gradient. The two trapped condensates are separated by a distance d. The atoms are coupled to the magnetic fields through their magnetic dipoles.

large detuning [6]. The Hamiltonian H_I describes the internal states and their interactions between the magnetic fields and is given by [6]

$$H_I = \hbar \sum_{\alpha=L,R} \left[\omega_e n_{e\alpha} + \omega_g n_{g\alpha} + \frac{\Omega_\alpha}{2}(e^{i\omega t} e_\alpha^\dagger g_\alpha + \text{H.c.}) \right], \tag{2}$$

where ω_e and ω_g are the frequencies of the atoms in states $|e\rangle$ and $|g\rangle$, respectively, and ω is the frequency of the magnetic field. The parameter Ω_L (Ω_R) is the coupling strength between the atoms and magnetic field B_L (B_R) in the left (right) potential well.

We work in the interaction picture by performing the unitary transformation as

$$U(t) = \exp\left[-it \sum_{\alpha=L,R} (\omega n_{e\alpha} + \omega_g n_{g\alpha}) \right]. \tag{3}$$

The transformed Hamiltonian becomes

$$H_I = \hbar \sum_{\alpha=L,R} \left[\Delta n_{e\alpha} + \frac{\Omega_\alpha}{2}(e_\alpha^\dagger g_\alpha + \text{H.c.}) \right], \tag{4}$$

where $\Delta = \omega_e - \omega$ is the detuning between the atoms and the magnetic field.

If the two wells are separated by a large distance, then the tunneling strengths are effectively turned off, i.e., $E_J^e = E_J^g = 0$. Here we consider the number of atoms in each trap to be equal to $N/2$, where N is the total number of atoms. For convenience, the system can be expressed in terms of angular momentum operators as [29]

$$J_{\alpha x} = \frac{1}{2}(e_\alpha^\dagger g_\alpha + g_\alpha^\dagger e_\alpha), \tag{5}$$

$$J_{\alpha y} = \frac{1}{2i}(e_\alpha^\dagger g_\alpha - g_\alpha^\dagger e_\alpha), \tag{6}$$

$$J_{\alpha z} = \frac{1}{2}(e_\alpha^\dagger e_\alpha - g_\alpha^\dagger g_\alpha), \tag{7}$$

where $\alpha = L,R$. The Hamiltonians H_0 and H_I are rewritten as

$$H_0 = \hbar \sum_{\alpha=L,R} \left[\frac{1}{2}(U_{ee} - U_{gg}) N J_{\alpha z} + \chi J_{\alpha z}^2 \right], \tag{8}$$

$$H_I = \hbar \sum_{\alpha=L,R} (\Delta J_{\alpha z} + \Omega_\alpha J_{\alpha x}), \tag{9}$$

where $\chi = U_{ee} + U_{gg} - 2U_{eg}$. We have omitted a constant term $\hbar(U_{ee}N^2 + U_{gg}N^2 + 2U_{eg}N^2 + 4\Delta N)/8$.

III. DETECTION OF MAGNETIC-FIELD GRADIENT

We present a scheme for detecting the magnetic-field gradient by using a pair of entangled BECs. First, it is necessary to generate the entanglement between two spatially separated condensates. Then, one of the condensates can be brought to another place for detection, and the atoms are coupled to the magnetic fields. The magnetic-field gradient can be estimated by measuring the variances of the population differences and relative phases between the condensates in the two internal states. The procedure of this detection scheme is described in the following subsections.

A. Generation of entangled states

To enhance the sensitivity of detection, it is necessary to generate the entanglement between the two separate condensates. We consider the condensates to be prepared in an entangled state, which is given by [16]

$$|\Psi_{\text{in}}\rangle = \frac{1}{\sqrt{2j+1}} \sum_m (-1)^m |j,m\rangle_L |j,-m\rangle_R, \tag{10}$$

where $|j,m\rangle_\alpha$ is an eigenstate of angular momentum operator $J_{\alpha z}$ for $\alpha = L,R$, and $j = N/4$. The spin states of the two condensates are anticorrelated [18].

Now we discuss how to generate the entangled state $|\Psi_{\text{in}}\rangle$ in Eq. (10). Initially, the atoms in the two different internal states $|e\rangle$ and $|g\rangle$ are confined in the different potential wells, where each condensate has an equal number of atoms, $N/2$. The initial Fock state can be prepared by appropriately controlling the strengths of atom-atom interactions and the tunneling strengths [21,30–32]. The intra- and intercomponent interaction strengths are tuned to be the same, i.e., $U \approx U_{ee} \approx U_{gg} \approx U_{eg}$. The tunneling strengths $E_J \approx E_J^e \approx E_J^g$ are much weaker than the atomic interaction strengths U. The entanglement between the atoms in the two components can be dynamically produced via the process of tunneling [18]. In this process, the atoms in the two different internal states can tunnel as a pair due to the strong atom-atom interactions. The entangled state can then be generated as [18]

$$|\Psi(t^*)\rangle \approx \sum_n c_n |n\rangle_{g_L} |N/2-n\rangle_{g_R} |N/2-n\rangle_{e_L} |n\rangle_{e_R}, \tag{11}$$

where c_n is the probability amplitude. When the population difference between the wells for each component condensate is about zero at time t^*, the probability amplitude c_n is approximately equal to $1/\sqrt{N/2+1}$. Then, the tunneling can be effectively switched off by adiabatically separating the two wells. Since the number of atoms in each well is equal, the

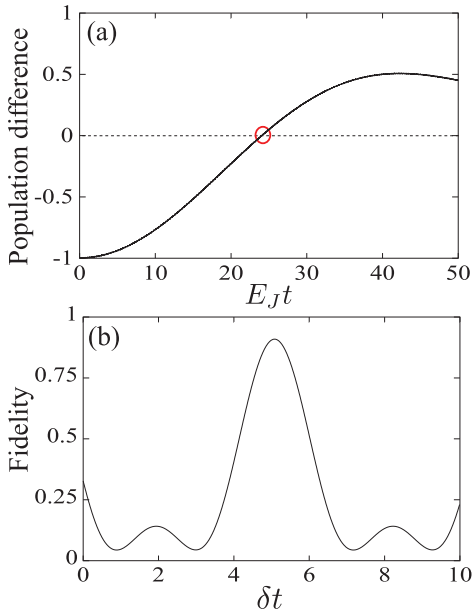

FIG. 2. (Color online) (a) Time evolution of the population difference between two wells vs time for the atoms in state $|g\rangle$. (b) Fidelity between the input state $|\Psi_{\rm in}\rangle$ and state $|\psi(t)\rangle$ vs time. The red circle denotes the zero-population difference between the two wells at time t^*. The following parameters are used: $N = 4$, $U = 10E_J$, $\delta_L = \delta$, and $\delta_R = 0$.

two-component condensate in each trap can be effectively described by an angular momentum system. Therefore, state $|\Psi(t^*)\rangle$ can be rewritten as [18]

$$|\Psi(t^*)\rangle \approx \frac{1}{\sqrt{2j+1}}\sum_m |n\rangle_{g_L}|N/2-n\rangle_{e_L}|N/2-n\rangle_{g_R}|n\rangle_{e_R}$$
$$\approx \frac{1}{\sqrt{2j+1}}\sum_m |j,m\rangle_L|j,-m\rangle_R, \qquad (12)$$

where $|j,m\rangle_L = |n\rangle_{g_L}|N/2-n\rangle_{e_L}$ and $|j,-m\rangle_R = |N/2-n\rangle_{g_R}|n\rangle_{e_R}$ are the eigenstates of J_{Lz} and J_{Rz}, respectively.

In Fig. 2(a), we plot the population difference between the two wells versus time, where the atoms are in $|g\rangle$. A red circle denotes the time t^* at which the population difference is equal to zero. The atoms in $|g\rangle$ can tunnel to the other well even if the interaction strengths U are much stronger than E_J.

The entangled state $|\Psi(t^*)\rangle$ in Eq. (12) differs from the entangled state $|\Psi_{\rm in}\rangle$ in Eq. (10) in the relative phases between the atoms. A relative phase shift can be accumulated by turning on the interaction, which can be described by the Hamiltonian $H_{\rm rp}$ as

$$H_{\rm rp} = \hbar(\delta_L J_{Lz} + \delta_R J_{Rz}), \qquad (13)$$

where δ_L is not equal to δ_R. State $|\psi(t)\rangle$ can be produced as

$$|\psi(t)\rangle = \exp\left(-\frac{i}{\hbar}H_{\rm rp}t\right)|\Psi(t^*)\rangle. \qquad (14)$$

This interaction can be made by controlling the strength U_{ee} and U_{gg} in Eq. (8) in one of the potential wells. Note that this interaction will not change the population difference between the two-component condensates. Therefore, the quantum numbers m in Eq. (12) remain unchanged during the interaction.

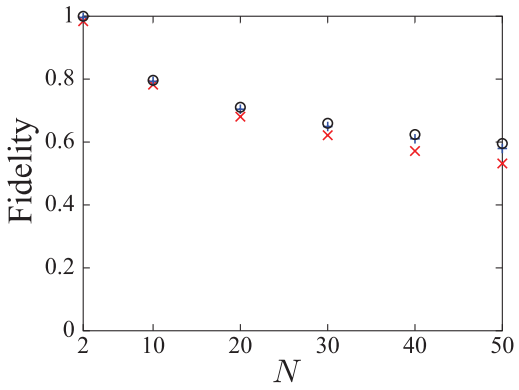

FIG. 3. (Color online) Fidelity between the input state $|\Psi_{\rm in}\rangle$ and the entangled state $|\tilde{\Psi}\rangle$ vs the total number N of atoms. The fidelities are shown with different parameters for generating $|\tilde{\Psi}\rangle$: $U = 5E_J$ (red crosses), $10E_J$ (blue pluses), and $50E_J$ (black circles).

After turning on the interaction for a specific time, the required entangled state $|\tilde{\Psi}\rangle$ can then be produced, where $|\tilde{\Psi}\rangle$ is the state which has the maximum fidelity [33] between $|\Psi_{\rm in}\rangle$ and $|\psi(t)\rangle$.

We then study the fidelity between states $|\Psi_{\rm in}\rangle$ and $|\psi(t)\rangle$. In Fig. 2(b), we plot the fidelity $|\langle\Psi_{\rm in}|\psi(t)\rangle|^2$ versus the time, where $\delta_L = \delta$ and $\delta_R = 0$. The fidelity varies with time t, as shown in Fig. 2(b). The highest fidelity can exceed 0.9.

In addition, we examine the fidelity between states $|\Psi_{\rm in}\rangle$ and $|\tilde{\Psi}\rangle$ for different numbers N of atoms in Fig. 3. As N increases, the fidelities decrease. However, a higher fidelity can be obtained with a higher ratio of U to E_J.

B. Coupling to the magnetic field

We consider the atoms to be coupled to the magnetic field at resonance, i.e., $\Delta = 0$ and setting $U_{ee} = U_{gg}$. Here we assume that the strengths of atom-atom interactions are much weaker than the coupling strengths Ω_L and Ω_R, and therefore they are ignored here. The effect of the atom-atom interactions will be discussed later. The Hamiltonian H_I reads

$$H_I = \hbar(\Omega_L J_{Lx} + \Omega_R J_{Rx}). \qquad (15)$$

The magnetic coupling strengths Ω_L and Ω_R are different from each other. Let us write $\Omega_L = \Omega + \Omega_D/2$ and $\Omega_R = \Omega - \Omega_D/2$. The Hamiltonian H_I can be written as

$$H_1 = \hbar\Omega(J_{Lx} + J_{Rx}) + \frac{\hbar\Omega_D}{2}(J_{Lx} - J_{Rx}). \qquad (16)$$

This small parameter Ω_D is to be determined.

C. Readout process

The magnetic-field gradient can be estimated by measuring the variance $\langle\tilde{J}_{yz}^2\rangle = \langle J_{y-}^2 - J_{z+}^2\rangle$, where $J_{y-} = J_{Ly} - J_{Ry}$ and $J_{z+} = J_{Lz} + J_{Rz}$. Physically speaking, $\langle J_{\alpha y}\rangle$ and $\langle J_{\alpha z}\rangle$ are the expectation values of the relative phase and population difference between the two-component condensates in potential well α, for $\alpha = L, R$. The variance $\langle\tilde{J}_{yz}^2\rangle$ is given by

$$\left\langle\tilde{J}_{yz}^2(\phi_D)\right\rangle = \frac{N(N+4)}{12}\cos(\phi_D), \qquad (17)$$

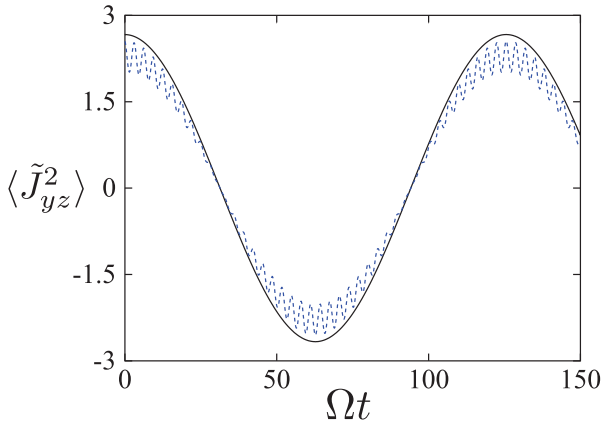

FIG. 4. (Color online) The variances $\langle \tilde{J}_{yz}^2 \rangle$ are plotted vs time for $N = 4$ and $\Omega_D = 0.05\,\Omega$. The black solid and blue dotted lines show the two different initial states, $|\Psi_{\rm in}\rangle$ and $|\tilde{\Psi}\rangle$, respectively, where $U = 10E_J$ is used to produce $|\tilde{\Psi}\rangle$.

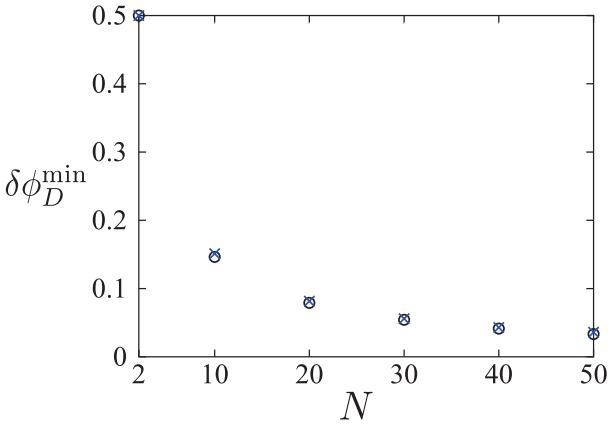

FIG. 5. (Color online) The minimum of the uncertainties $\delta\phi_D^{\rm min}$ vs the total number N of atoms for $\Omega_D = 0.05\,\Omega$. The empty circles and blue crosses denote the system with the two different initial states, $|\Psi_{\rm in}\rangle$ and $|\tilde{\Psi}\rangle$, respectively, where $U = 10E_J$ is used to produce state $|\tilde{\Psi}\rangle$.

where $\phi_D = \Omega_D t$. Here $\langle J_{y-}\rangle$ and $\langle J_{z+}\rangle$ are equal to zero for the input state $|\Psi_{\rm in}\rangle$ in Eq. (10). The expectation value $\langle \tilde{J}_{yz}^2(\phi_D)\rangle$ is a function of the parameter ϕ_D. Therefore, this quantity can be used for determining the magnetic-field gradient Ω_D. In Fig. 4, we plot the variance $\langle \tilde{J}_{yz}^2 \rangle$ versus the time for two different initial states, $|\Psi_{\rm in}\rangle$ and $|\tilde{\Psi}\rangle$. The variances $\langle \tilde{J}_{yz}^2 \rangle$ oscillate with the frequency ϕ_D for these two initial states. But the variance $\langle \tilde{J}_{yz}^2 \rangle$ shows some small-amplitude fluctuations in the oscillations if the initial state $|\tilde{\Psi}\rangle$ is used.

D. Sensitivity of detection

The magnetic-field gradient can be estimated from the variance $\langle \tilde{J}_{yz}^2 \rangle$. The uncertainty of the parameter ϕ_D is given by

$$\delta\phi_D = \frac{\Delta \tilde{J}_{yz}^2}{|\partial\langle \tilde{J}_{yz}^2\rangle/\partial\phi_D|}, \tag{18}$$

where $\Delta \tilde{J}_{yz}^2 = \sqrt{\langle \tilde{J}_{yz}^4\rangle - \langle \tilde{J}_{yz}^2\rangle^2}$. The uncertainty $\delta\phi_D$ can be found as

$$\delta\phi_D = \sqrt{\frac{15\sin^2(\phi_D) + (N-2)(N+6)\cos^2(\phi_D)}{5N(N+4)\sin^2(\phi_D)}}. \tag{19}$$

At time $t = \pi/2\Omega_D$, the minimum uncertainty $\delta\phi_D^{\rm min}$ is

$$\delta\phi_D^{\rm min} = \sqrt{\frac{3}{N(N+4)}}. \tag{20}$$

The uncertainty scales with $1/N$ for large N. Thus, the accuracy of the measurement can reach the Heisenberg limit [10].

In Fig. 5, we plot the minimum uncertainties $\delta\phi_D^{\rm min}$ versus the total number of atom, for the two different initial states $|\Psi_{\rm in}\rangle$ and $|\tilde{\Psi}\rangle$, respectively. The measurement using the two different initial states can give the similar values of $\delta\phi_D^{\rm min}$. Therefore, the entangled state $|\tilde{\Psi}\rangle$ can provide a similar accuracy of the case using the input state $|\Psi_{\rm in}\rangle$ in Eq. (10).

IV. EFFECT OF ATOM LOSSES

Now we study the sensitivity of the detection in the presence of one-body and two-body atom losses.

A. One-body atom loss

Here we study the one-body atom losses by using the phenomenological master equation [22,23]. The master equation describes one-body atom losses and can be written as [22,23]

$$\dot{\rho} = i[\rho, H] + \sum_{\alpha,\beta} \frac{\gamma_\beta^o}{2}(2\beta_\alpha\rho\beta_\alpha^\dagger - \beta_\alpha^\dagger\beta_\alpha\rho - \rho\beta_\alpha^\dagger\beta_\alpha), \tag{21}$$

where γ_β^o is the damping rate of one-body atom loss and $\alpha = L, R$ and $\beta = e, g$.

We compare the two estimators $\langle \tilde{J}_{yz}^2 \rangle$ and $\langle J_z^2 \rangle$ for determining the parameter ϕ_D in the presence of one-body atom loss, where $J_z = J_{Lz} + J_{Rz}$ is the sum of the population difference between the two hyperfine spin states of condensates in the two wells. In Fig. 6(a), we plot the variance $\langle \tilde{J}_{yz}^2 \rangle$ versus time for the different damping rates $\gamma^o = \gamma_e^o = \gamma_g^o$.

The initial state is $|\Psi_{\rm in}\rangle$ in Eq. (10). We can see that the variances $\langle \tilde{J}_{yz}^2 \rangle$ intersect at the same point at time $t = n\pi/2\Omega_D$, where n is an odd number. The parameter Ω_D can be estimated in the vicinity of these intersection points. In fact, the minimum uncertainty of the parameter Ω_D can be obtained at the first intersection point, i.e., $t = \pi/2\Omega_D$.

In Fig. 6(b), the variances $\langle J_z^2 \rangle$ are plotted versus time for the different damping rates γ^o. For $\gamma^o = 0$, the variance $\langle J_z^2 \rangle$ can be used to determine the parameter Ω_D [17]. However, the estimators $\langle J_z^2 \rangle$ do not intersect at the same point for the different damping rates γ^o. Further, the atom losses cause the shifts of the oscillations. This means that $\langle J_z^2 \rangle$ is not a faithful estimator for determining the parameter Ω_D in the presence of atom losses.

In Fig. 7, we plot the minimum uncertainties $\delta\phi_D^{\rm min}$ versus the total number N of atoms, where N is up to 10. Here the minimum uncertainties $\delta\phi_D^{\rm min}$ are obtained at time $t = \pi/2\Omega_D$. For comparison, the case using uncorrelated atoms without any

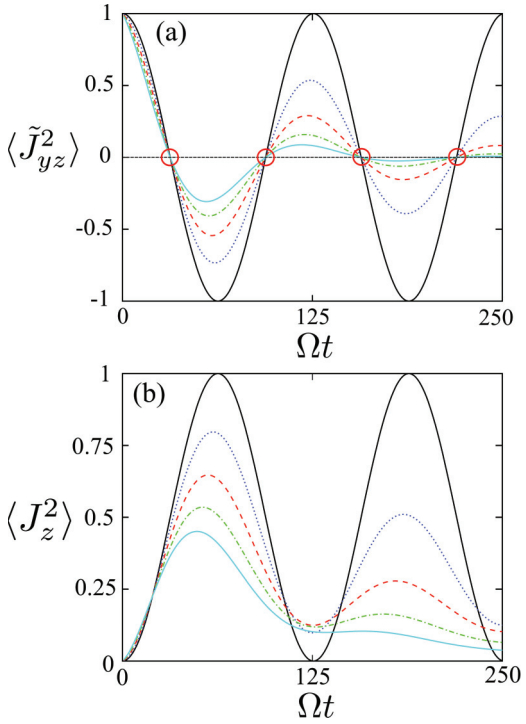

FIG. 6. (Color online) (a) Variances $\langle \tilde{J}_{yz}^2 \rangle$ vs time. (b) Variances $\langle J_z^2 \rangle$ vs time. The initial state is the entangled state $|\Psi_{\text{in}}\rangle$ in Eq. (10). The following parameters are used: $\Omega_D = 0.05\,\Omega$ and $N = 2$. Different damping rates are shown: $\gamma^o = 0$ (black solid line), $0.0025\,\Omega$ (blue dotted line), $0.005\,\Omega$ (red dashed line), $0.0075\,\Omega$ (green dot-dashed line) and $0.01\,\Omega$ (cyan solid line), respectively. The red circles denote the intersection points at $\langle \tilde{J}_{yz}^2 \rangle = 0$.

atom loss is also shown (green diamonds in Fig. 7), where the uncertainty is equal to $1/\sqrt{N}$ [10]. In Fig. 7, the entangled atoms can give a better performance than the uncorrelated atoms in the detection if the damping rate γ^o is much smaller than $\Omega_D = 0.05\,\Omega$. When $\gamma^o = 0.01\,\Omega$ becomes comparable to Ω_D, the accuracy of the detection is similar to the case using uncorrelated atoms, as shown in Fig. 7.

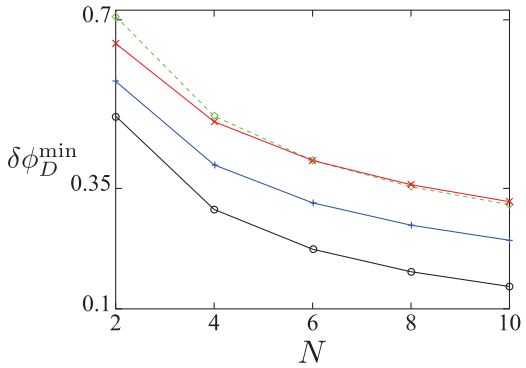

FIG. 7. (Color online) The minimum uncertainties $\delta\phi_D^{\min}$ plotted vs N for $\Omega_D = 0.05\,\Omega$. Different damping rates are shown: $\gamma^o = 0$ (black circles), $0.005\,\Omega$ (blue pluses), and $0.01\,\Omega$ (red crosses). The green diamonds (dashed line) denote the case using uncorrelated atoms with the uncertainty $1/\sqrt{N}$ for $\gamma^o = 0$.

B. Two-body atom loss

The phenomenological master equation describes two-body atom losses and can be written as [24]

$$\dot{\rho} = i[\rho, H] + \frac{\gamma_{ee}^t}{2} \sum_{\alpha=L,R} \left(2e_\alpha^2 \rho e_\alpha^{\dagger 2} - e_\alpha^{\dagger 2} e_\alpha^2 \rho - \rho e_\alpha^{\dagger 2} e_\alpha^2\right) + \frac{\gamma_{eg}^t}{2} \sum_{\alpha=L,R} (2e_\alpha g_\alpha \rho e_\alpha^\dagger g_\alpha^\dagger - e_\alpha^\dagger e_\alpha g_\alpha^\dagger g_\alpha \rho - \rho e_\alpha^\dagger e_\alpha g_\alpha^\dagger g_\alpha), \tag{22}$$

where the parameters γ_{ee}^t and γ_{eg}^t are the damping rates of two-body atom losses for the condensates in the upper internal state $|e\rangle$ and the atoms in the two different components and $\alpha = L, R$.

We plot the estimators $\langle \tilde{J}_{yz}^2 \rangle$ versus time for different damping rates γ_{eg}^t of two-body atom losses and $\gamma_{ee}^t = 0$ in Fig. 8(a) and $\gamma_{ee}^t = 1.5\gamma_{eg}^t$ [25] in Fig. 8(b). Both results show that $\langle \tilde{J}_{yz}^2 \rangle$ intersect at times $n\pi/2\Omega_D$, where n is an odd number. Therefore, the parameter Ω_D can be estimated at times $n\pi/2\Omega_D$ in the presence of two-body atom losses.

In Fig. 9, we plot the minimum uncertainties $\delta\phi_D^{\min}$ versus N, where the minimum uncertainties are taken at time $t = \pi/2\Omega_D$. The uncertainties from the measurement with uncorrelated atoms are shown with green diamonds, where

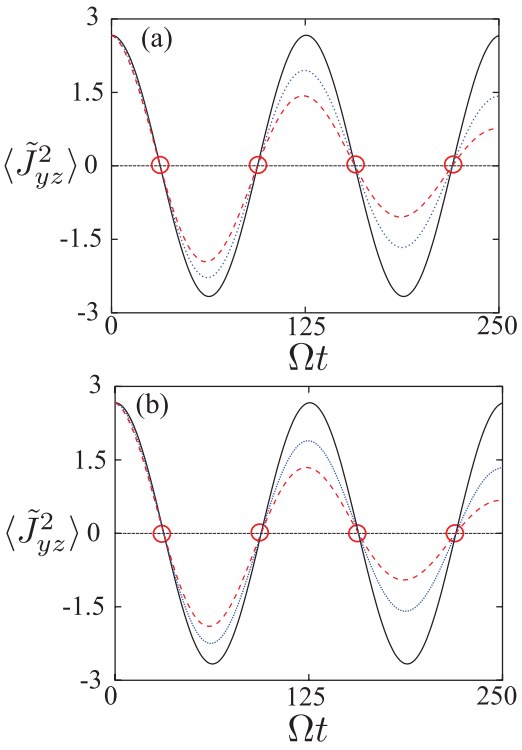

FIG. 8. (Color online) Variances $\langle \tilde{J}_{yz}^2 \rangle$ vs time. (a) Different damping rates are shown: $\gamma_{eg}^t = 0$ (black solid line), $0.005\,\Omega$ (blue dotted line), and $0.01\,\Omega$ (red dashed line), with $\gamma_{ee}^t = 0$. (b) Different damping rates are shown: $\gamma_{eg}^t = 0$ (black solid line), $0.001\,\Omega$ (blue dotted line), and $0.002\,\Omega$ (red dashed line), with $\gamma_{ee}^t = 1.5\gamma_{eg}^t$. The initial state is the input state $|\Psi_{\text{in}}\rangle$. The following parameters are used: $\Omega_D = 0.05\,\Omega$ and $N = 4$. The red circles denote the intersection points at $\langle \tilde{J}_{yz}^2 \rangle = 0$.

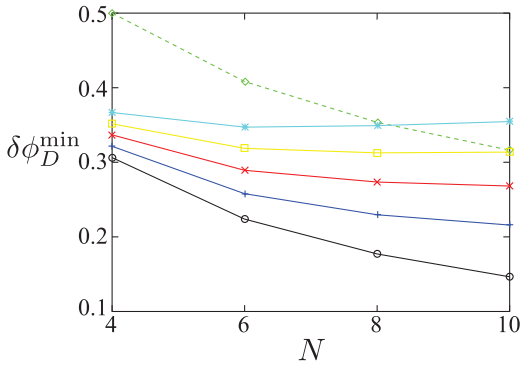

FIG. 9. (Color online) The minimum uncertainties $\delta\phi_D^{\min}$ vs N for $\Omega_D = 0.05\Omega$. Different damping rates γ_{eg}^t are shown: $\gamma_{eg}^t = 0$ (black circles), 0.0025Ω (blue plus), 0.005Ω (red crosses), 0.0075Ω (yellow squares), and 0.01Ω (cyan stars). The green diamonds (dashed line) denote the uncertainty $1/\sqrt{N}$ by using uncorrelated atoms without any atom loss.

$\gamma_{eg}^t = \gamma_{ee}^t = 0$. The parameters $\delta\phi_D^{\min}$ have different scalings with N for different rates γ_{eg}^t and $\gamma_{ee}^t = 0$. For small γ_{eg}^t, the entangled atoms can outperform the uncorrelated atoms for detection. When $\gamma_{eg}^t \geqslant 0.0075\,\Omega$ and $N \geqslant 8$, the uncertainty $\delta\phi_D^{\min}$ does not decrease with N. To obtain good performance of the measurements, the damping rates γ_{eg}^t have to be much smaller than the coupling strength of the magnetic-field gradient.

Next, we study the sensitivity of the detection by including the two-body atom loss for the atoms in the excited states in $|e\rangle$ [25]. In Fig. 10, we plot the minimum uncertainty $\delta\phi_D^{\min}$ versus N, where the minimum uncertainties are taken at time $t = \pi/2\,\Omega_D$. Here we set $\gamma_{ee}^t = 1.5\gamma_{eg}^t$ [25]. The minimum uncertainty exceeds the case of using uncorrelated atoms when γ_{eg}^t is equal to $0.002\,\Omega$. In this case, the two-body atom losses become more detrimental to the performance of the detection.

V. EFFECT OF ATOM-ATOM INTERACTIONS

We investigate the effect of the atom-atom interactions on the detection of magnetic-field gradient. In Fig. 11, we plot the variances $\langle \tilde{J}_{yz}^2 \rangle$ versus time for different nonlinear interaction strengths χ. When $\chi N \ll \Omega_D$, $\langle \tilde{J}_{yz}^2(t) \rangle$ are close to each other for different strengths χ. If the nonlinear interaction strength χ increases, then the amplitude of oscillations decreases, as shown in Fig. 11. In addition, the variances $\langle \tilde{J}_{yz}^2(t) \rangle$, for $\chi N \ll \Omega_D$, almost meet at the same points $\langle \tilde{J}_{yz}^2 \rangle = 0$ at times $t = n\pi/2\Omega_D$, where n is an odd number. At times $n\pi/2\Omega_D$, these give the minimum uncertainty of the parameter ϕ_D.

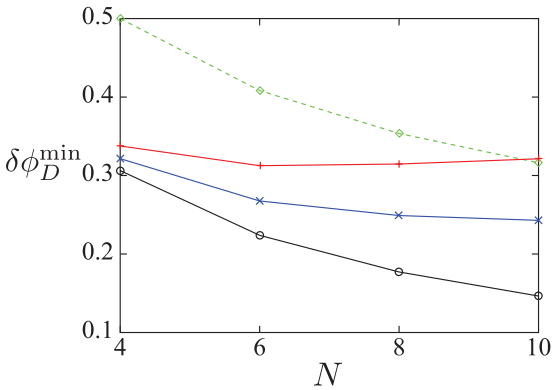

FIG. 10. (Color online) The minimum uncertainties $\delta\phi_D^{\min}$ vs N for $\Omega_D = 0.05\,\Omega$. Different damping rates are shown: $\gamma_{eg}^t = 0$ (black circles), $\gamma_{eg}^t = 0.001\,\Omega$ (blue crosses), and $\gamma_{eg}^t = 0.002\,\Omega$ (red pluses) for $\gamma_{ee}^t = 1.5\,\gamma_{eg}^t$. The green diamonds (dashed line) denote the case of using uncorrelated atoms with the uncertainty $1/\sqrt{N}$.

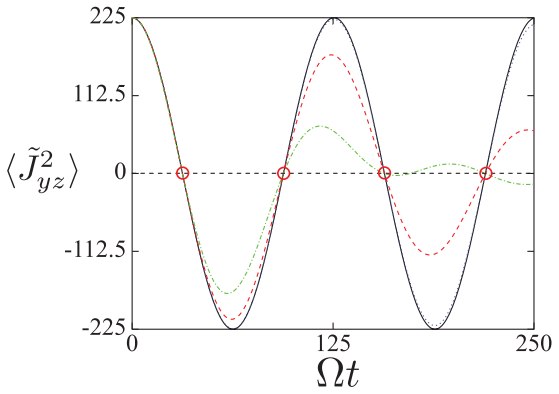

FIG. 11. (Color online) Time evolution of variances $\langle \tilde{J}_{yz}^2 \rangle$ for different strengths of atom-atom interactions: $\chi = 0$ (black solid line), $10^{-4}\,\Omega$ (blue dotted line), $5 \times 10^{-4}\,\Omega$ (red dashed line), and $0.001\,\Omega$ (green dot-dashed line). The following parameters are used: $N = 50$ and $\Omega_D = 0.05\,\Omega$. The red circles denote the intersection points at $\langle \tilde{J}_{yz}^2 \rangle = 0$.

Next, we investigate the uncertainty $\delta\phi_D^*$ at time $t = \pi/2\Omega_D$. In Fig. 12, we plot the uncertainties $\delta\phi_D^*$ versus N for different nonlinear interaction strengths χ. The uncertainty $\delta\phi_D^*$ is close to the minimum uncertainty $\delta\phi_D^{\min}$ for $\chi N \ll \Omega_D$. When χ increases, the uncertainty $\delta\phi_D^*$ does not decrease for larger N, as shown in Fig. 12. Therefore the strong nonlinear interactions limit the performance of detection.

In fact, the effects of nonlinear interactions can be minimized by setting $\chi N \ll \Omega_D$. The nonlinear interaction strength can be appropriately adjusted by using Feshbach resonance [11] and a state-dependent trap [12].

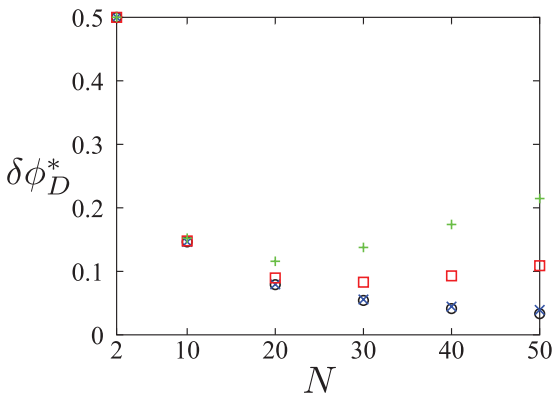

FIG. 12. (Color online) The uncertainties $\delta\phi_D^*$ are plotted vs N for $\delta\Omega_D = 0.05\,\Omega$. Different strengths of atom-atom interactions are shown: $\chi = 0$ (black circles), $10^{-4}\,\Omega$ (blue crosses), $5 \times 10^{-4}\,\Omega$ (red squares), and $0.001\,\Omega$ (green pluses).

VI. DISCUSSION

Let us make some remarks on our method for detecting the magnetic-field gradient by using ^{87}Rb atoms. The transition frequency of ^{87}Rb atoms can be tuned by using an external static magnetic field [6]; the range of the frequencies of the detected magnetic field is about a few gigahertz to 10 GHz [6,34].

Next, we roughly estimate the magnitude of the magnetic-field gradient, which can be probed by using the condensates. Indeed, the measurement is mainly limited by the atom loss rate of the condensates. The main source comes from two-body atom losses [25]. The two-body loss rate is $(\gamma_{eg}^t + \gamma_{ee}^t)N/V$, where γ_{eg}^t $(\gamma_{ee}^t) \sim 10^{-13}$ cm^3 s^{-1} [25] and V is the volume of the condensate. The rates of two-body atom losses depend on the density of the atomic gases. We assume that V is about $(1\ \mu\text{m})^3$. The rates of two-body atom loss range from 1 to 10 Hz for $N = 10$ to 100. To obtain good performance, the coupling strength of the magnetic-field gradient Ω_D must be much larger than the two-body atom loss rates. The coupling strength $\Omega_{L(R)}$ between the two states is about $\mu_B B_{L(R)}/\hbar$ [6], where μ_B is the Bohr magneton. Thus, the minimum value of the magnetic field can be detected in the range of 10^{-10} to 10^{-9} T for $N = 10$ to 100 and $V = (1\ \mu\text{m})^3$. The minimum value of the detectable magnetic-field gradient is about 10^{-9}–10^{-10} T.

VII. CONCLUSION

In summary, we have proposed a method to detect the magnetic-field gradient by using entangled condensates. We have described how to generate entangled states of two spatially separated condensates. The magnetic-field gradient can be determined by measuring the variances of relative phases and population differences between the two-component condensates in the two wells. The uncertainty of the parameter scales with $1/N$. We have also numerically studied the effects of one-body and two-body atom losses on the detection. We show that the entangled atoms can outperform the uncorrelated atoms in detecting the magnetic fields for a few atoms. The effect of atom-atom interactions on this method has also been discussed.

ACKNOWLEDGMENTS

We thank Shih-I Chu. This work was supported in part by National Basic Research Program of China Grants No. 2011CBA00300 and No. 2011CBA00301 and National Natural Science Foundation of China Grants No. 61073174, No. 61033001, and No. 61061130540.

[1] D. Budker and M. Romalis, Nat. Phys. **3**, 227 (2007).
[2] Y. S. Greenberg, Rev. Mod. Phys. **70**, 175 (1998).
[3] M. Hämääinen, R. Hari, R. J. Ilmoniemi, J. Knuutila, and O. V. Lounasmaa, Rev. Mod. Phys. **65**, 413 (1993).
[4] S. Wildermuth, S. Hofferberth, I. Lesanovsky, S. Groth, P. Krger, and J. Schmiedmayer, Appl. Phys. Lett. **88**, 264103 (2006).
[5] M. Vengalattore, J. M. Higbie, S. R. Leslie, J. Guzman, L. E. Sadler, and D. M. Stamper-Kurn, Phys. Rev. Lett. **98**, 200801 (2007).
[6] P. Böhi, M. F. Riedel, T. W. Hänsch, and P. Treutlein, Appl. Phys. Lett. **97**, 051101 (2010).
[7] D. M. Harber, H. J. Lewandowski, J. M. McGuirk, and E. A. Cornell, Phys. Rev. A **66**, 053616 (2002).
[8] P. Treutlein, P. Hommelhoff, T. Steinmetz, T. W. Hänsch, and J. Reichel, Phys. Rev. Lett. **92**, 203005 (2004).
[9] R. Horodecki, P. Horodecki, M. Horodecki, and K. Horodecki, Rev. Mod. Phys. **81**, 865 (2009).
[10] V. Giovannetti, S. Lloyd, and L. Maccone, Science **306**, 1330 (2004).
[11] C. Gross, T. Zibold, E. Nicklas, J. Estevbe, and M. K. Oberthaler, Nature (London) **464**, 1165 (2010).
[12] M. F. Riedel, P. Böhi, Y. Li, T. W. Hänsch, A. Sinatra, and P. Treutlein, Nature (London) **464**, 1170 (2010).
[13] H. T. Ng and Shih-I Chu, Phys. Rev. A **84**, 023629 (2011).
[14] P. Hommelhoff, W. Hänsel, T. Steinmetz, T. W. Hänsch, and J. Reichel, New J. Phys. **7**, 3 (2005).
[15] A. Sørensen, L.-M. Duan, J. I. Cirac, and P. Zoller, Nature (London) **409**, 63 (2001).
[16] H. Cable and G. A. Durkin, Phys. Rev. Lett. **105**, 013603 (2010).
[17] I. Urizar-Lanz, P. Hyllus, I. L. Egusquiza, M. W. Mitchell, and G. Tóth, arXiv:1203.3797.
[18] H. T. Ng, C. K. Law, and P. T. Leung, Phys. Rev. A **68**, 013604 (2003).
[19] M. Albiez, R. Gati, J. Fölling, S. Hunsmann, M. Cristiani, and M. K. Oberthaler, Phys. Rev. Lett. **95**, 010402 (2005).
[20] S. Fölling, S. Trotzky, P. Cheinet, M. Feld, R. Saers, A. Widera, T. Müller, and I. Bloch, Nature (London) **448**, 1029 (2007).
[21] J. Estève, C. Gross, A. Weller, S. Giovanazzi, and M. K. Oberthaler, Nature (London) **455**, 1216 (2008).
[22] J. J. Cooper, D. W. Hallwood, and J. A. Dunningham, Phys. Rev. A **81**, 043624 (2010).
[23] J. J. Cooper, D. W. Hallwood, J. A. Dunningham, and J. Brand, Phys. Rev. Lett. **108**, 130402 (2012).
[24] A. M. Rey, L. Jiang, and M. D. Lukin, Phys. Rev. A **76**, 053617 (2007).
[25] K. M. Mertes, J. W. Merrill, R. Carretero-Gonzàlez, D. J. Frantzeskakis, P. G. Kevrekidis, and D. S. Hall, Phys. Rev. Lett. **99**, 190402 (2007).
[26] J. Grond, U. Hohenester, I. Mazets, and J. Schmiedmayer, New J. Phys. **12**, 065036 (2010).
[27] I. Tikhonenkov, M. G. Moore, and A. Vardi, Phys. Rev. A **82**, 043624 (2010).
[28] G. J. Milburn, J. Corney, E. M. Wright, and D. F. Walls, Phys. Rev. A **55**, 4318 (1997).
[29] J. J. Sakurai, *Modern Quantum Mechanics* (Addison-Wesley, Reading, MA, 1994).
[30] C. Orzel, A. K. Tuchman, M. L. Fenselau, M. Yasuda, and M. A. Kasevich, Science **291**, 2386 (2001).
[31] G. B. Jo, Y. Shin, S. Will, T. A. Pasquini, M. Saba, W. Ketterle, D. E. Pritchard, M. Vengalattore, and M. Prentiss, Phys. Rev. Lett. **98**, 030407 (2007).
[32] W. Li, A. K. Tuchman, H.-C. Chien, and M. A. Kasevich, Phys. Rev. Lett. **98**, 040402 (2007).
[33] A. Uhlmann, Rep. Math. Phys. **9**, 273 (1976); R. Jozsa, J. Mod. Opt. **41**, 2315 (1994).
[34] D. A. Steck, Rubidium 87 D line data, http://steck.us/alkalidata/.